



# Locating hydrothermal acoustic sources at Old Faithful Geyser using Matched Field Processing

Estelle Cros, Philippe Roux, Jean Vandemeulebrouck, S. Kedar

## ► To cite this version:

Estelle Cros, Philippe Roux, Jean Vandemeulebrouck, S. Kedar. Locating hydrothermal acoustic sources at Old Faithful Geyser using Matched Field Processing. *Geophysical Journal International*, 2011, 187 (1), pp.385-393. 10.1111/J.1365-246X.2011.05147.X . hal-00624592

**HAL Id: hal-00624592**

**<https://hal.science/hal-00624592>**

Submitted on 19 Sep 2011

**HAL** is a multi-disciplinary open access archive for the deposit and dissemination of scientific research documents, whether they are published or not. The documents may come from teaching and research institutions in France or abroad, or from public or private research centers.

L'archive ouverte pluridisciplinaire **HAL**, est destinée au dépôt et à la diffusion de documents scientifiques de niveau recherche, publiés ou non, émanant des établissements d'enseignement et de recherche français ou étrangers, des laboratoires publics ou privés.

# Locating hydrothermal acoustic sources at Old Faithful Geyser using Matched-Field Processing

E. Cros<sup>1</sup>, P. Roux<sup>2</sup>, J. Vandemeulebrouck<sup>1</sup>  
and S. Kedar<sup>3</sup>

<sup>1</sup> ISTerre, CNRS UMR5275, Université de Savoie, Campus Scientifique,  
73376 Le Bourget-du-Lac Cedex, France

<sup>2</sup> ISTerre, CNRS UMR5275, Université Joseph Fourier,  
Maison des Géosciences, BP 53,  
38041 Grenoble Cedex 9, France

<sup>3</sup> Jet Propulsion Laboratory, California Institute of Technology,  
Pasadena, CA 91109, USA

## 1 Summary

In 1992, a large and dense array of geophones was placed around the geyser vent of Old Faithful, in the Yellowstone National Park, in order to determine the origin of the seismic hydrothermal noise recorded at the surface of the geyser and to understand its dynamics. Old Faithful Geyser (OFG) is a small-scale hydrothermal system where a two-phase flow mixture erupts every 40 to 100 minutes in a high continuous vertical jet. Using Matched Field Processing (MFP) techniques on 10-min-long signal, we localize the source of the seismic pulses recorded at the surface of the geyser. Several MFP approaches are compared in this study, the frequency-incoherent and frequency coherent approach, as well as the linear Bartlett processing and the non-linear Minimum Variance Distorsionless Response (MVDR) processing. The different MFP techniques used give the same source position with better focalization in the case of the MVDR processing. The retrieved source position corresponds to the geyser conduit at a depth of 12 m and the localization is in good agreement with in-situ measurements made at Old Faithful in past studies.

Keywords: Hydrothermal systems ; Volcano seismology ; Wave propagation ; North America

## 2 Introduction

Old Faithful Geyser (OFG) is located in the Upper Geyser Basin (UGB) in the Yellowstone National Park. The basin is approximately  $3.2 \times 0.8$  km and is on the periphery of the Mallard Lake resurgent dome within the Yellowstone Caldera. The caldera was formed 640,000 years ago by a giant eruption and measures  $80 \times 50$  km. The presence of a

complex magmatic reservoir system beneath the caldera (Fournier, 1989; Husen et al., 2004; Miller & Smith, 1999) delivers the heat that maintain the hot springs, geysers and mud pots on the different basins. The heat flux density calculated with a river chloride inventory method is estimated at  $2000 \text{ mW m}^{-2}$  over the  $2900 \text{ km}^2$  corresponding to the caldera area (Fournier, 1989). The Yellowstone thermal water is mainly meteoric in origin with magmatic contribution less than a few percent (Fournier, 1989).

The edifice of OFG is essentially conical with a diameter of 60 m, and is characterized by a 4 m high geyserite vent concretion, with an opening of  $2 \text{ m} \times 1 \text{ m}$ , and an irregular, elongated fissure-like conduit (Hutchinson et al., 1997). It is one of the most studied geyser in the world because of its regularity and the short interval between two eruptions which makes its study very convenient. The time interval between two eruptions follows a bimodal distribution, between 40 and 100 minutes, with a principal mode centered on 80 minutes. The eruption is characterized by a continuous vertical jet of water and steam at a height of 30 to 50 m lasting for 1 to 6 min for a total discharge of water between 14 000 and 32 000 l.

Most of the studies on Old Faithful focalize on the evolution of the time interval between two eruptions (Hurwitz et al., 2008; Rinehart, 1969), on the characterization of the seismic signals recorded around the vent (Kedar et al., 1996, 1998; Kieffer, 1984) or on the working-out of a dynamic model of the cycle (Hutchinson et al., 1997; Kieffer, 1984).

Kieffer (1984) was the first to give an elaborate description of the Old Faithful Geyser behaviour, including its seismicity and thermodynamics, based on the data collected by Birch and Kennedy in 1948. She established a model of the rise of water in the conduit before an eruption (Figure 1) and considered that the collapse of steam bubbles which cool in the upper part of the water column, is a major physical process that transfers latent heat to the water column, and produces impulsive acoustic events, which composed the seismic signal recorded at the surface. Hutchinson et al. (1997), using pressure probes and a small video camera lowered in the conduit, were able to observe different hydrodynamic processes occurring in the conduit, such as boiling, cavitation, but also superheated steam expansion, and exsolution of incondensable gas that they proposed to be  $\text{CO}_2$ . From 1991 to 1994, Kedar and colleagues conducted several seismic surveys at the surface simultaneously with pressure and temperature measurements in the OFG conduit (Kedar et al., 1996). During their experiment, an array of 96 short period vertical geophones, and several broadband sensors were placed around the geyser vent. At the surface they recorded a quasi harmonic seismic signal composed of the succession of very impulsive events. They observed that the tremor intensity is modulated by the variations in the conduit shape during water rise (Kedar et al., 1998). The impulsive events composing the signal recorded at the surface reverberate in a soft shallow layer and are not generated by resonance in the water column, as assumed by Kieffer (1984). Finally, pressure measurements in the conduit confirmed that the individual seismic pulses are generated by the collapse of bubbles.

The goal of this paper is to revisit the data recorded at OFG by Kedar and his colleagues with the dense array of geophones in order to check how acoustic source localization techniques derived from ocean acoustics, namely Matched Field Processing (MFP), can be used to localize the cavitation events recognized by Kieffer and Kedar in the conduit during the cycle.

MFP is a well-established passive technique used to track submarines or marine mam-

mals in the ocean, to differentiate animals or to understand their behaviour (Thode et al., 2000). MFP was recently tested with success on a seismic array of ten sensors deployed on hydrothermal systems, exhibiting the dominant acoustic source below the array (Legaz et al., 2009; Vandemeulebrouck et al., 2010). In the present case, the seismic array is six times denser than during the aforementioned experiments on hydrothermal systems. Moreover, the seismic sources are shallow and can be associated with in-situ measurements that provide additional constraints to this study.

### 3 Data

The network deployed by Kedar consists of 96 vertical 1 Hz geophones spread on a tight grid around the vent of the geyser (Figure 2). The 96 geophones originally recorded signal during several eruptions with a sampling frequency of 250 Hz, but only 10 minutes of signal were readily available to be processed in this study. Nevertheless, this 10-minute interval is associated with a stable stage of the geyser cycle, when the water level is slowly rising in the conduit approximately 20 minutes before the eruption (Kedar et al. (1998), see Figure 1). From the array data, a map of the seismic intensity radiated at the surface around the geyser was calculated at different periods during the cycle by Sharon Kedar (1996), and the results showed no significant behaviour. Several hammer shots were also performed to complete the study, in order to look at the difference between the excitation of the medium by the hammer shot and by the seismic natural impulsive sources.

Finally, the analysis of single seismic events recorded on the geophones with a simultaneous measurement of the water pressure in the water column at different depths was performed by Sharon Kedar (Kedar, 1996; Kedar et al., 1996, 1998). The fact that the record of a pressure pulse near the top surface is followed by the record of an impulsive event on the geophones clearly indicates that these events are generated by bubble collapses in the water column.

Thus, the seismic signal recorded in this study is mainly composed of impulsive events (Figures 3 a and c), with a duration in the order of 0.2 s and with an approximate rate of 100 events per minute (Figure 3 c). During an eruption, it was observed that the number of events before an eruption follows an asymptotical law (Kedar, 1996), corresponding to the rise of the water level in the conduit. The 10-min-long record processed in this study is mainly stable in amplitude and does not show evidence of an eruption (Figure 3 a). It actually corresponds to a period of approximately 20 minutes before an eruption. The frequency content of the signal is large with two modes, the first one, the most energetic, between 10 and 40 Hz and the second one, between 50 and 65 Hz (Figure 3 b).

## 4 Method

### 4.1 Presentation of the MFP techniques

In volcano seismology, source localization is generally performed on a series of single events of the same type (Very Long Period, Long Period, Volcano-Tectonic, Tremor). Historically, time-picking of arrival time has been performed on impulsive volcano-tectonics events. When this method cannot be used, several other methods exist to localize seismic

events recorded on volcanoes. Among these methods, cross-correlation technique permits to determine the time delays between pairs of station and to compare these delays with theoretical ones associated to a point source. This technique was applied to localize Long Period events on Mt Etna (De Barros et al., 2009). The source positions retrieved were in agreement with the localization given by time-reversal on these same events (O'Brien et al., 2011). The estimation of the slowness vector has also been applied on volcanic signals of different types in order to locate their origin (Almendros et al., 2001; Métaixian et al., 2002) as well as on the subduction zone in the Cascades (La Rocca et al., 2010) to retrieve the location of the tremor sources.

Similarly, one can retrieve the source location by looking at the spatial amplitude distribution for several types of events recorded across a network and comparing it with theoretical amplitude decay calculated for a given point source location. Assuming the type of waves considered, i.e. body waves or surface waves, we can retrieve the source location which best fits the data (Aki & Ferrazzini, 2000; Battaglia & Aki, 2003). The method was successfully applied on rockfalls but faced difficulties when considering Volcano-Tectonic events occurring below the summit of the volcano and below the sea level due to the complexity of the amplitude distribution in this region.

Another technique using a set of similar earthquakes or Long Period events, called multiplets, consists in determining the difference in origin times between each pair of events in the multiplet. Localization is then performed by minimizing the residuals between the time delays between two events and theoretical time delays computed after relative relocation (Battaglia et al., 2003; Got et al., 1994). Finally, the semblance method was used on tremors generated by a volcanic eruption in order to follow the migration of the seismic activity between two potential sources on Izu-Oshima Island volcano in Japan (Furumoto et al., 1990).

In geothermal areas, the seismic signal recorded at the surface of the hydrothermal system is composed of randomly distributed impulsive events related to bubble collapse (Ichihara & Nishimura, 2011; Kedar et al., 1998; Legaz et al., 2009; Vandemeulebrouck et al., 2010). In the case of the present data, the impulsive events often overlap and present very different signal-to-noise ratio on the geophone array at the surface. This makes time picking algorithms unefficient to identify and relocalize each event. Furthermore, the high rate of events (100 per minute, see Figure 3 c) would make an event-by-event relocalization very time consuming. In this perspective, the advantage of the Matched Field Processing (MFP) technique is to build up a probability of presence of the dominant acoustic source on a selected time window of the recorded signals. As a matter of fact, the goal of MFP is to stack the events on a time interval  $T$  in order to provide a robust relative phase measurement on the whole array. In other words, under the approximation that most of the bubble collapses in the time window  $T$  come from the same area (within the half-wavelength), the MFP capitalizes on the phase coherence of these events recorded on the array. Thus, MFP cumulates the advantage of (1) a better signal-to-noise ratio through the stacking of events in the time interval  $T$  and (2) an automatic procedure to localize the dominant seismic source as a function of time for long recordings.

Historically, MFP is a localization technique commonly used in ocean acoustics that starts to be used on hydrothermal systems. This array processing method is a generalization of beamforming techniques in the sense that it basically compares phase delays of forward modeling solutions of the wave equation to acquired data. More precisely, MFP

consists in placing a test source at each point of a 3-D search grid, computing the acoustic field at all elements of the array and then matching this modelled field with the data. The match is maximum when a point source of the search grid is co-located with the true point source. The result of the processing is a probability map of the source position.

There exist different ways to match the modelled field to the data. The linear method, called Bartlett MFP, performs a correlation between the data and the model. The non-linear method, in our case the Minimum-Variance Distorsionless Response (MVDR), computes a maximum-likelihood type minimization between the data and the model. Compared to Bartlett, the MVDR technique improves the resolution of the MFP output but it requires both a good signal-to-noise ratio on the recorded data and a propagation model that perfectly adjusts to the data (Jensen et al., 1995). On the other hand, the Bartlett MFP gives a robust solution, even for low signal-to-noise ratio, with a spatial resolution that is limited to the acoustic wavelength according to diffraction laws.

For both linear and non-linear MFP algorithms, the processing is performed in the frequency domain as follows.

First, the cross-spectral density matrix (CSDM)  $K$  is calculated as:

$$K = d \cdot d^* \quad (1)$$

with  $d = [d_f^1, d_f^2, \dots, d_f^N]$  defined as the acoustic signal at frequency  $f$  recorded on a geophone  $i$  ( $i$  varying from 1 to  $N$  geophones). The star indicates the complex conjugate transpose operation.

Second, a model-based replica vector  $d_m(f, a_i)$  is defined at frequency  $f$  as the modelled field from a candidate source position to the array elements, with  $a_i$  being the vector corresponding to the absolute distance between the source candidate position and geophone  $i$  of the array. In our case, the propagation model corresponds to the free-space medium which means that the replica vector is expressed by:

$$d_m(f, a_i) = \frac{1}{4\pi a_i} \exp\left(\frac{-2\pi i f a_i}{c}\right). \quad (2)$$

In Eq. 2, the free-space monopolar Green's function is chosen as the replica vector since we expect to retrieve a local source for which the geophone array is located at one or two wavelengths away from the source. In this case, the separation between Rayleigh waves and body waves is not effective and wave propagation can be modelled by a velocity  $c$  that depends on the medium physical properties. Because of the simple form of the replica vector in Eq. 2, MFP could also be described as spherical beamforming. However, more complex Green's function could be used as replica vectors in the case of a forward model with layering, for example.

The linear MFP (Bartlett) processor is estimated as follows:

$$B_{Bart}(a_i) = \sum_{j=1}^L |d_m^*(f_j, a_i) \cdot K(f_j) \cdot d_m(f_j, a_i)|. \quad (3)$$

Similarly, the non-linear processor (MVDR) output is formulated as:

$$B_{MV}(a_i) = \sum_{j=1}^L \left| \frac{1}{d_m^*(f_j, a_i) \cdot K^{-1}(f_j) \cdot d_m(f_j, a_i)} \right|. \quad (4)$$

As shown in Eqs. 3 and 4 above, the MFP is typically averaged incoherently over a set of frequencies  $f_1, f_2, \dots, f_L$  in order to improve the contrast of the MFP output.

However, the MFP can be processed coherently by considering the cross-correlation field instead of the acoustic noise data to construct the cross-spectral density matrix  $K$ . The coherent use of MFP implies a coherent average over a discrete number of frequencies in the bandwidth of interest, which requires the source signal to be isolated in the data. This is done by cross-correlating the noise signal recorded on each element of the array to a reference geophone (Figure 4). The coherent approach can be used in two ways. The first considers correlations associated with one reference geophone only, then separately calculates the MFP using the correlations with different geophones and averages the different MFP outputs. A better approach consists in (1) calculating all correlations between the geophones and (2) selecting a set of  $p$  correlations that correspond to an homogeneous distribution of station pairs among the network, i.e. the inter-station paths cover uniformly the whole area (Figure 8 c).

To consider a coherent MFP processing, the set of correlations are transformed into the frequency domain as data vectors at frequencies  $f_1, f_2, \dots, f_L$ . We then create a “supervector”  $\hat{d}$ :

$$\hat{d} = [d_{f_1}^1, d_{f_1}^2, \dots, d_{f_1}^p, \dots, d_{f_L}^1, \dots, d_{f_L}^p], \quad (5)$$

where  $p$  is the number of correlation functions selected among the geophone array. The CSDM is calculated as before:

$$\hat{K} = \hat{d} \cdot \hat{d}^*. \quad (6)$$

Since the data are now issued from correlations between sensor pairs at different frequencies, the replica vectors have to follow the same logic. This means that the replica vector is expressed by:

$$\hat{d}_m(f, a_i, a_{ref}) = \frac{1}{16\pi^2 a_i a_{ref}} \exp\left(\frac{-2\pi i f (a_i - a_{ref})}{c}\right). \quad (7)$$

where  $a_i$  and  $a_{ref}$  refer now to the distance between the candidate source position and, respectively, the  $i$  th geophone or the reference geophone. The model-based replica is then compiled into a “supervector”  $\hat{d}_m$  equivalent to the data “supervector” from which the linear and non linear coherent MFP are computed as:

$$B_{Bart}(\hat{a}_i) = |\hat{d}_m^*(a_i) \cdot \hat{K} \cdot \hat{d}_m(a_i)|; \quad (8)$$

$$B_{MV}(\hat{a}_i) = \left| \frac{1}{\hat{d}_m^*(a_i) \cdot \hat{K}^{-1} \cdot \hat{d}_m(a_i)} \right|. \quad (9)$$

It has been shown that the coherent MFP yields better results than the incoherent approach for tracking objects in the ocean (Debever & Kuperman, 2007; Michalopoulou & Porter, 1996). The disadvantage of coherent processing is that it requires the manipulation of large matrices which may considerably increase the computation time.

Moreover, a fundamental requirement for MFP processing is that the signal recorded at the sensors is coherent from one geophone to another. This often limits its application to low frequency as will be shown in the next section. A good first guess is required of the medium velocity, especially for the MVDR where small speed mismatch can degrade the resolution of the source localization. Two standards are used to evaluate the MFP result:

(1) focalization (size of the focal spot) and (2) contrast (ratio between the maximum of the MFP output and eventual sidelobes).

## 4.2 Processing

The first step in the MFP processing is the selection of the appropriate frequency bandwidth. A few points have to be taken into considerations. First, the higher the frequency, the shorter the wavelength and the better the spatial resolution of the MFP localization. MFP is based on the spatial coherence of the recorded signals, which tends to decrease at higher frequencies and limits the use of large arrays. Furthermore, MFP always applies a comparison between the data and a wave propagation model. The higher the frequency, the more complicated the model must be since short wavelengths are typically more sensitive to spatial heterogeneities. Finally, the propagation model used for MFP in the case of a broad frequency bandwidth must also include a frequency-dependent velocity profile. A balance between MFP resolution at high frequencies and robust MFP localization at low frequencies is problem-specific and must be determined on a case by case basis.

In the case of Old Faithful data, the spatial coherence was first calculated from 8 to 70 Hz. The coherency is high between 12 and 58 Hz, while the signals are most energetic in the frequency band 10 to 40 Hz (Figure 3 b). Finally, comparing the MFP results in the 5-15 Hz and 20-30 Hz bands, it appeared that the focalization and the contrast are better in the lower frequency band. The MFP was then processed between 5 Hz and 15 Hz with a 1 Hz sliding frequency window, and the contrast and the focalization were optimal at 12 Hz.

In the second step, an estimation of the seismic velocity was performed using the records of 12 hammer shots made by Sharon Kedar in 1992. This analysis revealed that the mean surface velocity is  $\sim 130 \text{ ms}^{-1}$  between 11 and 13 Hz, with a low-velocity area in the South part of the network. This zone of lower velocity could be associated with softer sediments deposited in a small stream area. When performing MFP, we have used this mean surface velocity ( $130 \text{ ms}^{-1}$ ) in a 1-D tabular model. The vertical gradient was estimated from a velocity model of S. Kedar (1996) using shear waves velocity model, as shown in Figure 5 and is of  $23.5 \text{ ms}^{-1}/\text{m}$ .

In the final step, we selected the sensors to be used with the incoherent processing or the sensor pairs in the case of coherent processing. Sensors located in a lower velocity zone and showing a degraded spatial coherence were rejected (Figure 4). For coherent MFP processing, we restricted our choice to five reference stations among the network in order to (1) provide homogeneous spatial distribution of the station pairs while (2) limiting the size of the  $\hat{K}$  and thus the computation time of the MFP processing.

## 4.3 Results and discussion

The 10 minutes of recorded signal were processed in order to localize and monitor the dominant noise source position. The signals were truncated into chunks of  $T=20\text{s}$  time window from which coherent/incoherent MFP was performed using either the linear Bartlett or non-linear MVDR method.

Figures 6 and 7 shows incoherent MFP results for one  $T=20\text{s}$  time window using Bartlett and MVDR processing. The MFP results are displayed as 3-D maps that cor-



respond to the probability of presence of the noise source (Figures 6 a and 7 a). We first notice that both linear/non-linear MFP give the same general source position. The spatial resolution of the MFP is evaluated from slices in the X-Y, X-Z and Y-Z planes at the MFP maximum (Figures 6 b-d and 7 b-d). As expected, the incoherent MVDR performs better than the Bartlett in terms of spatial focalization. Indeed, the spatial resolution of the linear Bartlett MFP is limited to the half-wavelength ( $\sim 6.5$  m) according to diffraction laws while the non-linear MVDR MFP outpasses this limit with a  $\sim 2$  m spatial resolution.

When compared to incoherent MFP, coherent MFP does not improve the focalization results as shown in Figures 8 a and b. Compared to ocean where coherent processing significantly improved the focalization performance (Debever & Kuperman, 2007), the optimal focalization limit was already reached with incoherent MFP in this case thanks to the high signal-to-noise ratio of the seismic signals and the dense spatial coverage provided by the geophone array around the geyser vent.

To confirm the validity of the MFP results, travel times were calculated between the MFP source position and each sensor according to the velocity model plotted in Figure 5. When compared to a reference geophone, these theoretical time-delays were then superimposed to the cross-correlation function with the same reference geophone (Figure 4). The satisfactory adjustment of the theoretical time-delays with the dominant cross-correlation wavefront over most of the geophone array is an a posteriori validation of MFP results. The discrepancy observed for sensors 17 to 20 may be due to wrong station coordinates or to the presence of a strong spatial heterogeneity in the medium.

The 12-m depth of the noise source is consistent with in-situ observations (Hutchinson et al., 1997). The temperature measurements made by Birch & Kennedy (1972) indicate a stationarity of the water level in the conduit during the same cycle period, which was confirmed by Hutchinson et al. (1997). Furthermore, in-situ observations with a camera made by Hutchinson revealed the presence of a widening of the conduit between 10.5 and 14 m. The horizontal location of the source with the different MFP processors closely corresponds to the orifice position (Figures 8 a and b). The digression of the source position from the horizontal location of the vent maybe due to the widening of the conduit at depth. This shift could also be attributed to the uncertainty on the velocity model and the geophone positions.

The monitoring of the noise source inside the vent was performed for each successive  $T=20$ s time-window with an overlap of 75%. The spatial localization of the noise sources is shown in Figures 9 a-c, showing stable results during the 10-min-long recording. The standard deviation of the source position in the X and Y direction is 0.30 m, while standard deviation is slightly larger in the Z direction with a value of 0.42 m. More precisely, the source depth shows periodic variation with a dominant period slightly less than 1 minute (Figures 9 d and e). This period may be associated with temperature oscillation observed at this depth (Hutchinson et al., 1997), likely due to two-phase flow static instabilities (Bouré et al., 1973).

## 5 Conclusion

The efficiency of the MFP method was demonstrated in retrieving the location of the dominant noise source in hydrothermal systems.

277 Using a velocity model (Kedar, 1996) and the mean surface velocity calculated using  
278 hammer shots, the origin of the seismic signals recorded at Old Faithful Geyser on a  
279 geophone network at the surface is in good agreement with in-situ measurements. The  
280 dominant seismic source location during this period of record corresponds to a steady  
281 state with continuous boiling rate at a given constant depth ( $\sim 12$  m).

282 The data processing using different MFP techniques show similar source locations.  
283 Differences in the MFP results concern the spatial width of the focalization according to  
284 the MFP technique. The MVDR MFP proved to provide higher resolution results than  
285 the Bartlett MFP for all cases analyzed in this study, resulting in a  $\sim 2$  m source resolution  
286 for the MVDR MFP, compared to  $\sim 4$  m resolution for Bartlett MFP.

287 The time-evolution of the source location of the multiple impulsive events was continu-  
288 ously followed during a 10-min-long steady period of seismic activity and showed a stable  
289 source position, with fluctuations of small amplitude (less than 50 cm) and a period less  
290 than one minute. Applying MFP techniques on longer data set, comprising several cycles,  
291 would permit to perform a temporal monitoring of the acoustic source and to improve  
292 the understanding of the geyser dynamics.

293 Furthermore, the MFP method could be an interesting tool to monitor other volcanic  
294 signals like volcano-tectonic event (VT) or long period event (LP).

## 6 acknowledgments

Most of the computations presented on this article were performed at the Service Commun de Calcul Intensif de l'Observatoire de Grenoble (SCCI). The Digital Elevation Model used in this study is based on data services provided by the OpenTopography Facility with support from the National Science Foundation under NSF Award Numbers 0930731 and 0930643 and is based on services provided by the Plate Boundary Observatory operated by UNAVCO for EarthScope (<http://www.earthscope.org>) and supported by the National Science Foundation (No. EAR-0350028 and EAR-0732947). We would like to thank Shaul Hurwitz and Robert Clayton for their help.

## References

- Aki, K. & Ferrazzini, V., 2000. Seismic monitoring and modeling of an active volcano for prediction, *J. geophys. Res.*, **105**(B7), 16,617–16,640.
- Almendros, J., Chouet, B., & Dawson, P., 2001. Spatial extent of a hydrothermal system at Kilauea Volcano, Hawaii, determined from array analyses of shallow long-period seismicity. 1. Method, *J. geophys. Res.*, **106**(B7), 13565–13580.
- Battaglia, J. & Aki, K., 2003. Location of seismic events and eruptive fissures on the Piton de la Fournaise Volcano using seismic amplitudes, *J. geophys. Res.*, **108**(B8), 2364.
- Battaglia, J., Got, J.-L., & Okubo, P., 2003. Location of long-period events below Kilauea Volcano using seismic amplitudes and accurate relative relocation, *J. geophys. Res.*, **108**(B12), 2553.
- Birch, F. & Kennedy, G. C., 1972. Notes on geyser temperatures in Iceland and Yellowstone National Park, *Flow and fracture of rocks: American Geophysical Union Geophysical Monograph*, **16**, 329–336.
- Bouré, J., Bergles, A., & Tong, L., 1973. Review of two-phase flow instability, *Nuclear Engineering and Design*, **25**(2), 165–192.
- De Barros, L., Bean, C. J., Lokmer, I., Saccorotti, G., Zuccarello, L., O’Brien, G. S., Métaxian, J.-P., & Patanè, D., 2009. Source geometry from exceptionally high resolution long period event observations at Mt Etna during the 2008 eruption, *Geophys. Res. Lett.*, **36**(24), L24305.
- Debever, C. & Kuperman, W. A., 2007. Robust matched-field processing using a coherent broadband white noise constraint processor, *J. acoust. Soc. Am.*, **122**(4), 1979–1986.
- Fournier, R. O., 1989. Geochemistry and dynamics of the Yellowstone National Park hydrothermal system, *Annu. Rev. Earth planet. Sci.*, **17**(1), 13–53.
- Furumoto, M., Kunitomo, T., Inoue, H., Yamada, I., Yamaoka, K., Ikami, A., & Fukao, Y., 1990. Twin sources of high-frequency volcanic tremor of Izu-Oshima Volcano, Japan, *Geophys. Res. Lett.*, **17**(1), 25–27.
- Got, J.-L., Fréchet, J., & Klein, F. W., 1994. Deep fault plane geometry inferred from multiplet relative relocation beneath the south flank of Kilauea, *J. geophys. Res.*, **99**(B8), 15375–15386.
- Hurwitz, S., Kumar, A., Taylor, R., & Heasler, H., 2008. Climate-induced variations of geyser periodicity in Yellowstone National Park, USA, *Geology*, **36**(6), 451–454.
- Husen, S., Smith, R. B., & Waite, G. P., 2004. Evidence for gas and magmatic sources beneath the Yellowstone volcanic field from seismic tomographic imaging, *J. Volc. Geotherm. Res.*, **131**(3-4), 397–410.

- Hutchinson, R. A., Westphal, J. A., & Kieffer, S. W., 1997. In situ observations of Old Faithful Geyser, *Geology*, **25**(10), 875–878.
- Ichihara, M. & Nishimura, T., 2011. Pressure impulses generated by bubbles interacting with ambient perturbation, *Extreme Environmental Events*, pp. 731–752.
- Jensen, F. B., Kuperman, W. A., Porter, M. B., Schmidt, H., & Bartram, J. F., 1995. *Computational Ocean Acoustics*, American Institute of Physics, New York, (578 pp.).
- Kedar, S., 1996. *The origin of harmonic tremor at Old Faithful*, Ph.D. thesis, Caltech.
- Kedar, S., Sturtevant, B., & Kanamori, H., 1996. The origin of harmonic tremor at Old Faithful Geyser, *Nature*, **379**, 708–711.
- Kedar, S., Kanamori, H., & Sturtevant, B., 1998. Bubble collapse as the source of tremor at Old Faithful Geyser, *J. geophys. Res.*, **103**, 24,283–24,299.
- Kieffer, S. W., 1984. Seismicity at Old Faithful Geyser: an isolated source of geothermal noise and possible analogue of volcanic seismicity, *J. Volc. Geotherm. Res.*, **22**(1-2), 59-95.
- La Rocca, M., Galluzzo, D., Malone, S., McCausland, W., & Del Pezzo, E., 2010. Array analysis and precise source location of deep tremor in Cascadia, *J. geophys. Res.*, **115**, B00A20.
- Legaz, A., Revil, A., Roux, P., Vandemeulebrouck, J., Gouédard, P., Hurst, T., & Bolève, A., 2009. Self-potential and passive seismic monitoring of hydrothermal activity: A case study at Iodine Pool, Waimangu geothermal valley, New Zealand, *J. Volc. Geotherm. Res.*, **179**(1-2), 11 – 18.
- Métaxian, J.-P., Lesage, P., & Valette, B., 2002. Locating sources of volcanic tremor and emergent events by seismic triangulation: Application to Arenal volcano, Costa Rica, *J. geophys. Res.*, **107**(B10), 2243.
- Michalopoulou, Z.-H. & Porter, M. B., 1996. Matched-field processing for broad-band source localization, *IEEE Journal of Oceanic Engineering*, **21**, 384–392.
- Miller, D. S. & Smith, R. B., 1999. P and S velocity structure of the Yellowstone volcanic field from local earthquake and controlled-source tomography, *J. geophys. Res.*, **104**(B7), 15105–15121.
- O’Brien, G. S., Lokmer, I., De Barros, L., Bean, C. J., Saccorotti, G., Métaxian, J.-P., & Patané, D., 2011. Time reverse location of seismic long-period events recorded on Mt Etna, *Geophys. J. Int.*, **184**(1), 452–462.
- Rinehart, J., 1969. Old Faithful Geyser performance 1870 through 1966, *Bull. Volcanol.*, **33**(1), 153–163.
- Thode, A. M., D’Spain, G. L., & Kuperman, W. A., 2000. Matched-field processing, geoacoustic inversion, and source signature recovery of blue whale vocalizations, *J. acoust. Soc. Am.*, **107**(3), 1286–1300.

Vandemeulebrouck, J., Roux, P., Gouédard, P., Legaz, A., Revil, A., Hurst, A., Bolève, A., & Jardani, A., 2010. Application of acoustic noise and self-potential localization techniques to a buried hydrothermal vent (Waimangu Old Geyser site, New Zealand), *Geophys. J. Int.*, **180**(2), 883–890.

Figure 1 : Water level in the conduit of Old Faithful before an eruption reported by Birch & Kennedy (1972), from an adaptation of Kieffer (1984).

Figure 2 : (a) Shaded relief map of Old Faithful area. Coordinates are indicated in [m UTM]. (b) Topographic map and location of the 96 vertical 1 Hz geophones around the vent of Old Faithful Geyser. Elevation contour interval is one meter. The red square corresponds to the grid where the MFP was processed. The reference coordinates of the geyser vent are  $X=513,672.51$  m UTM,  $Y=4,923,032.42$  m UTM and  $Z=2240$  m.

Figure 3 : A 10-minute-long record at geophone 90. a): 10 minutes record. b): Average amplitude spectrum calculated over the 96 geophones. c): Zoom between 300 and 310 s.

Figure 4 : Cross-correlation of 10 minutes of seismic signal recorded on the 96 geophones with the sensor 54 as reference. The signals are bandpass filtered between 10 and 14Hz. The symbols correspond to theoretical delays associated with the point source retrieved with MFP ( $X=-1.35$  m,  $Y=1.65$  m and  $Z=11$  m) in a 1-D model with a vertical gradient of velocity of  $23.5 \text{ ms}^{-1}/\text{m}$  and a surface velocity of  $130 \text{ ms}^{-1}$ , the black stars indicate the sensors used for the processing and the magenta circles are associated to sensors that were disregarded in the MFP processing.

Figure 5 : A velocity model proposed by Kedar (1996) compared to the velocity model used for the localization.

Figure 6 : (a) 3-D Incoherent Bartlett output between 11.5 and 12.5 Hz for a medium with a velocity of  $130 \text{ ms}^{-1}$  at surface and a gradient of velocity of  $23.5 \text{ ms}^{-1}/\text{m}$ , with (b) slice in the plane X-Z, (c) slice in the plane Y-Z and (d) slice in the plane X-Y. The white circle corresponds to the horizontal vent location. The source was determined using the search grid represented on Figure 2 (b).

Figure 7 : (a) 3-D Incoherent MVDR output between 11.5 and 12.5 Hz for a medium with a velocity of  $130 \text{ ms}^{-1}$  at surface and a gradient of velocity of  $23.5 \text{ ms}^{-1}/\text{m}$ , with (b) slice in the plane X-Z, (c) slice in the plane Y-Z and (d) slice in the plane X-Y. The white circle corresponds to the horizontal vent location. The source was determined using the search grid represented in red on Figure 2 (b).

Figure 8 : Estimated locations of the seismic sources using the whole 10 minutes of signal according to the MFP method. Each error bar refers to the spot width measured at 70% of the maximum. The methods used are B: Bartlett and M: MVDR. These methods were processed (a): incoherently, (b): coherently with correlations calculated between 11.5 and 12.5 Hz from  $p=171$  station pairs. The dotted lines on gray represent the position of the vent at the surface. (c): Number of paths per cell projected on a  $70 \times 70$  m grid with 5-m squared cells around the geyser position for the stations pairs selected for the coherent MFP.

Figure 9 : (a) Location of the seismic sources in a X-Y plane during 10 minutes of signal determined with coherent Bartlett processed on 20-s-long-windows and with an overlap of 75% . The position of the source is relative to the position of the vent. (b) Location of the seismic sources on a X-Z plane and (c) on a Y-Z plane. (d) Location of the seismic source in depth according to the time. (e) Fourier Transform of the source position dynamics averaged on the X, Y and Z directions.

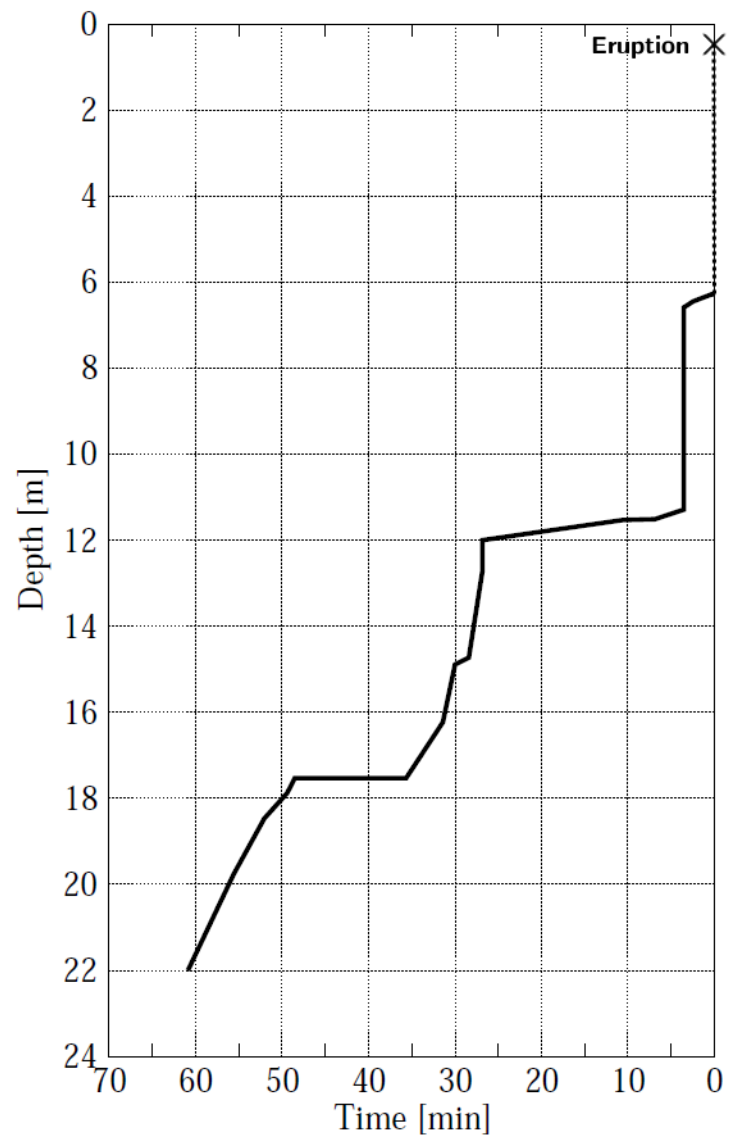


Figure 1



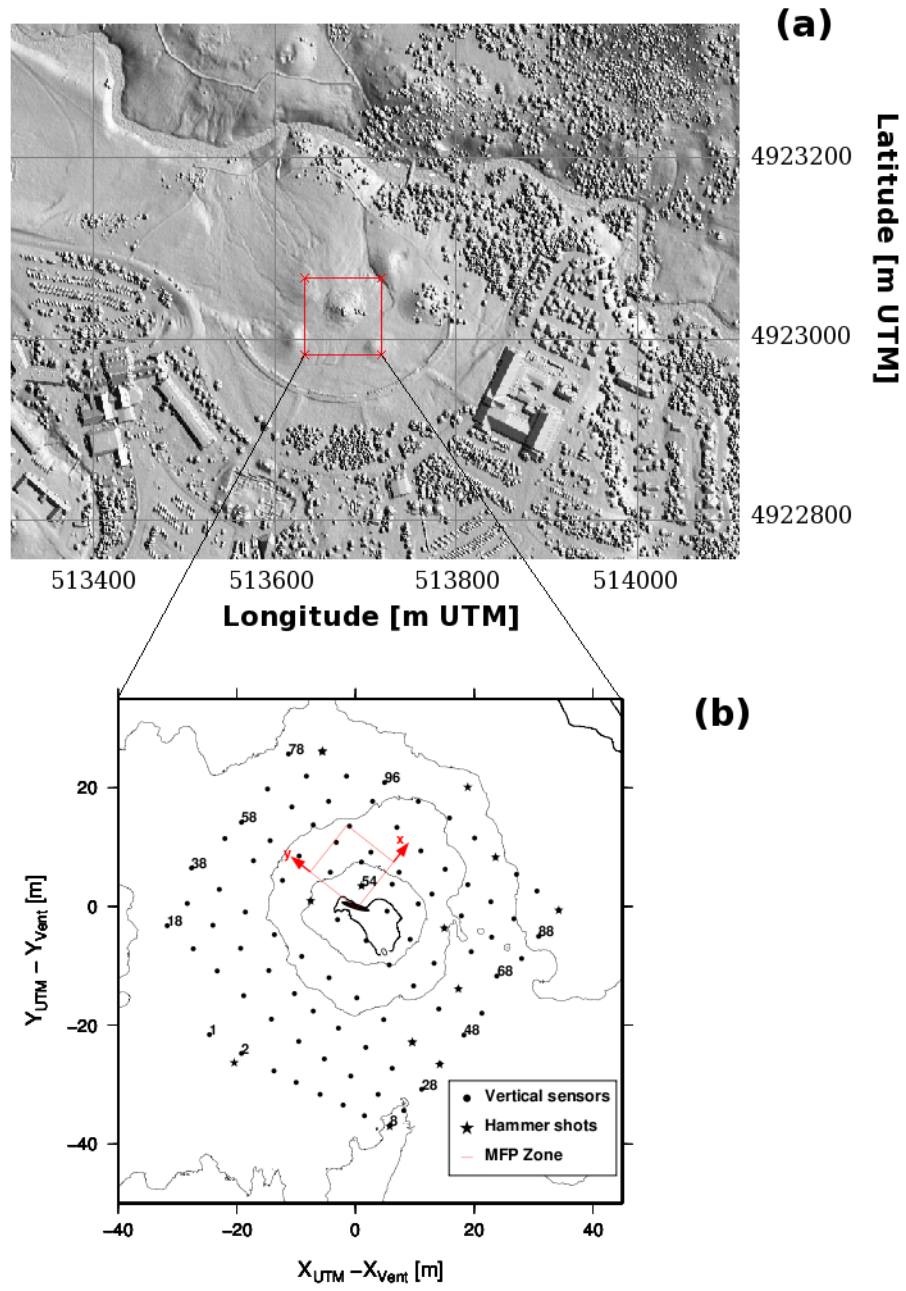


Figure 2

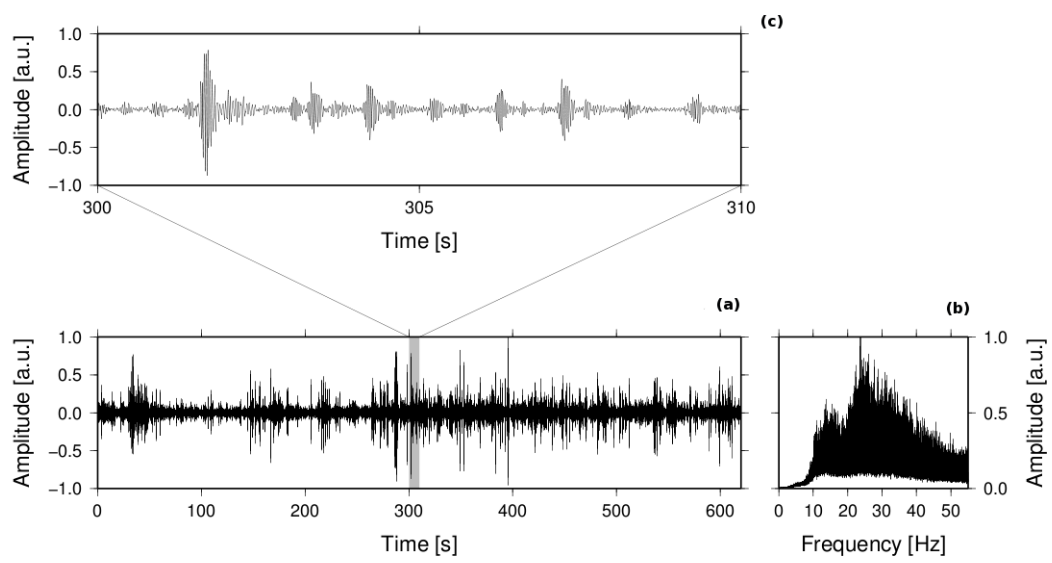


Figure 3

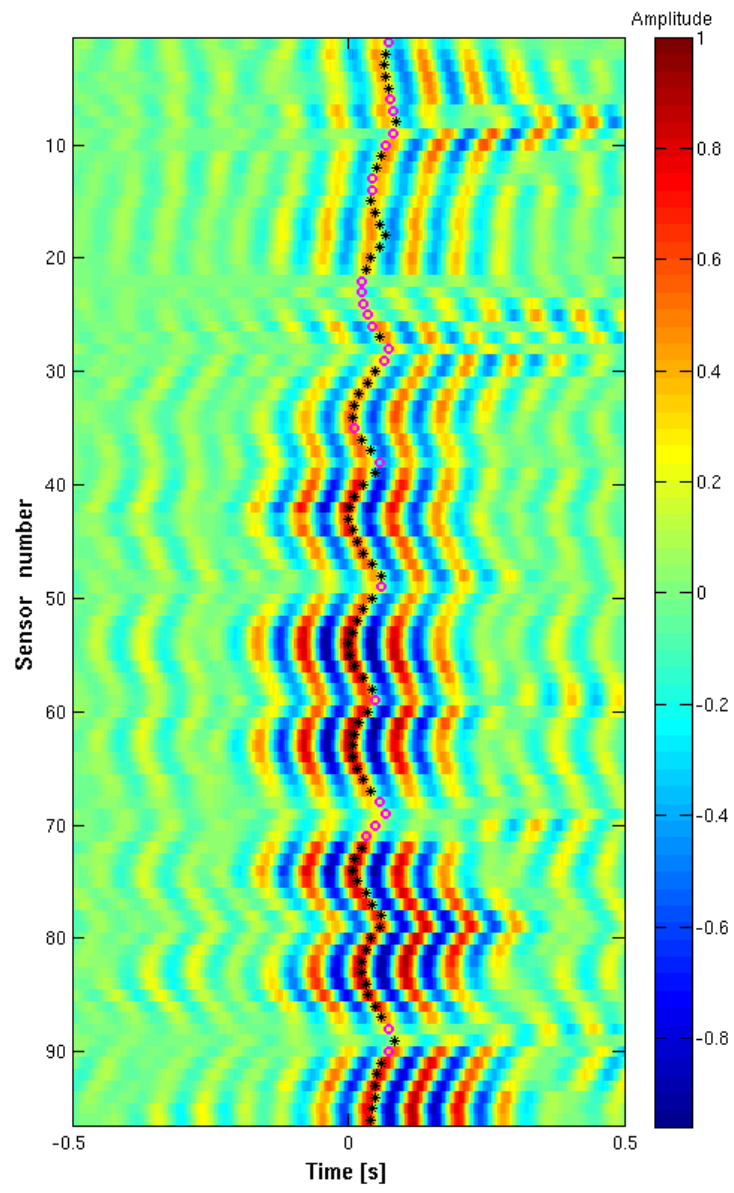


Figure 4

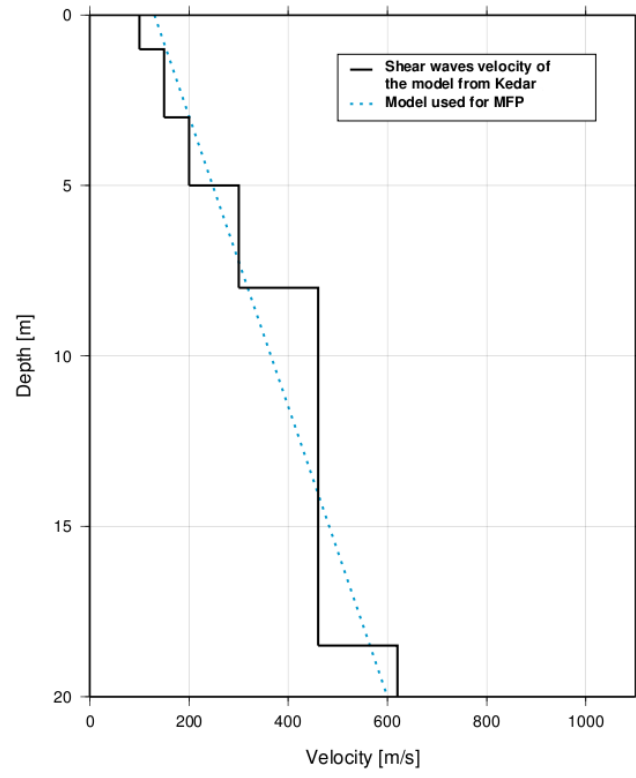


Figure 5

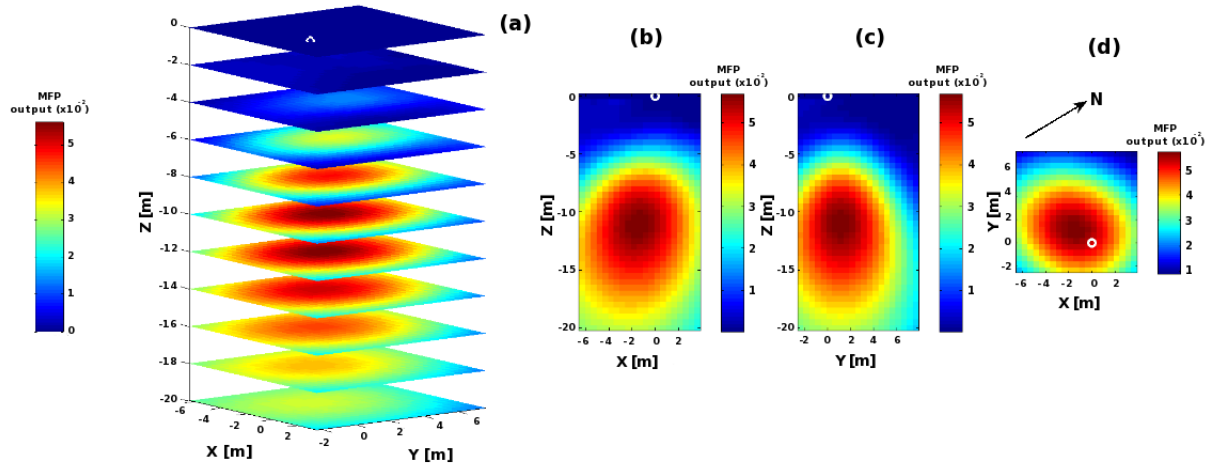


Figure 6

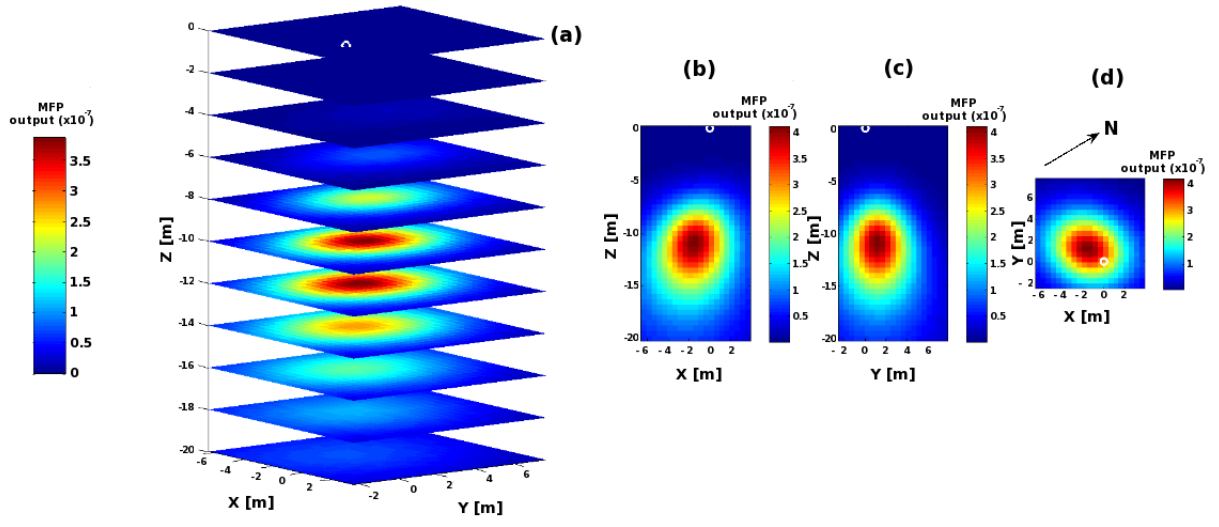


Figure 7

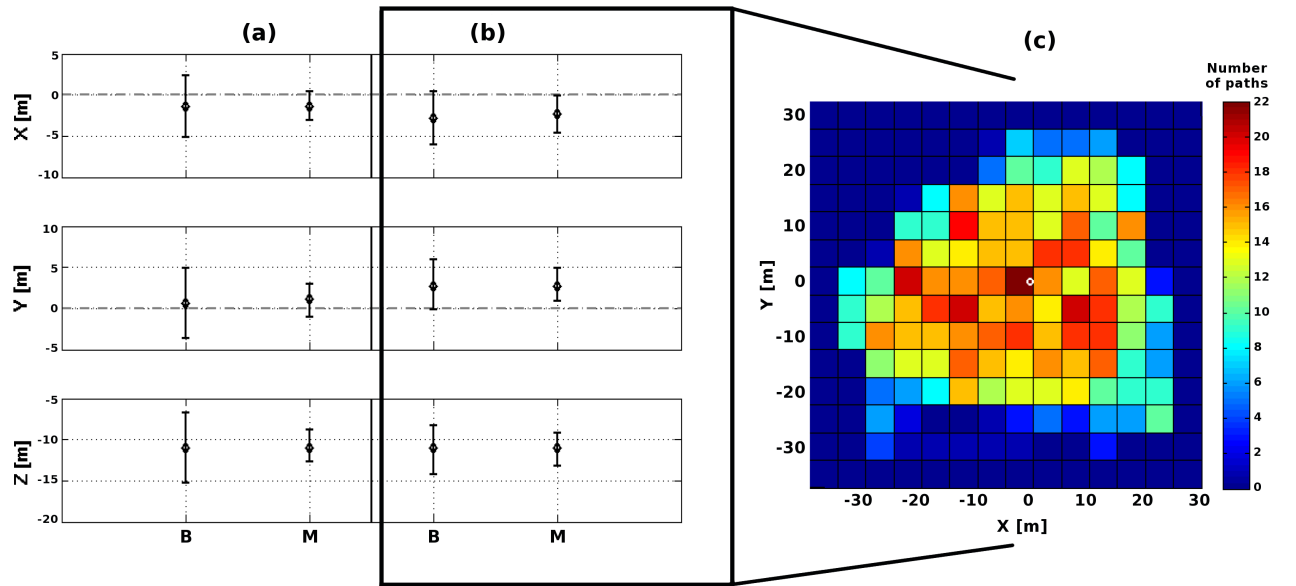


Figure 8

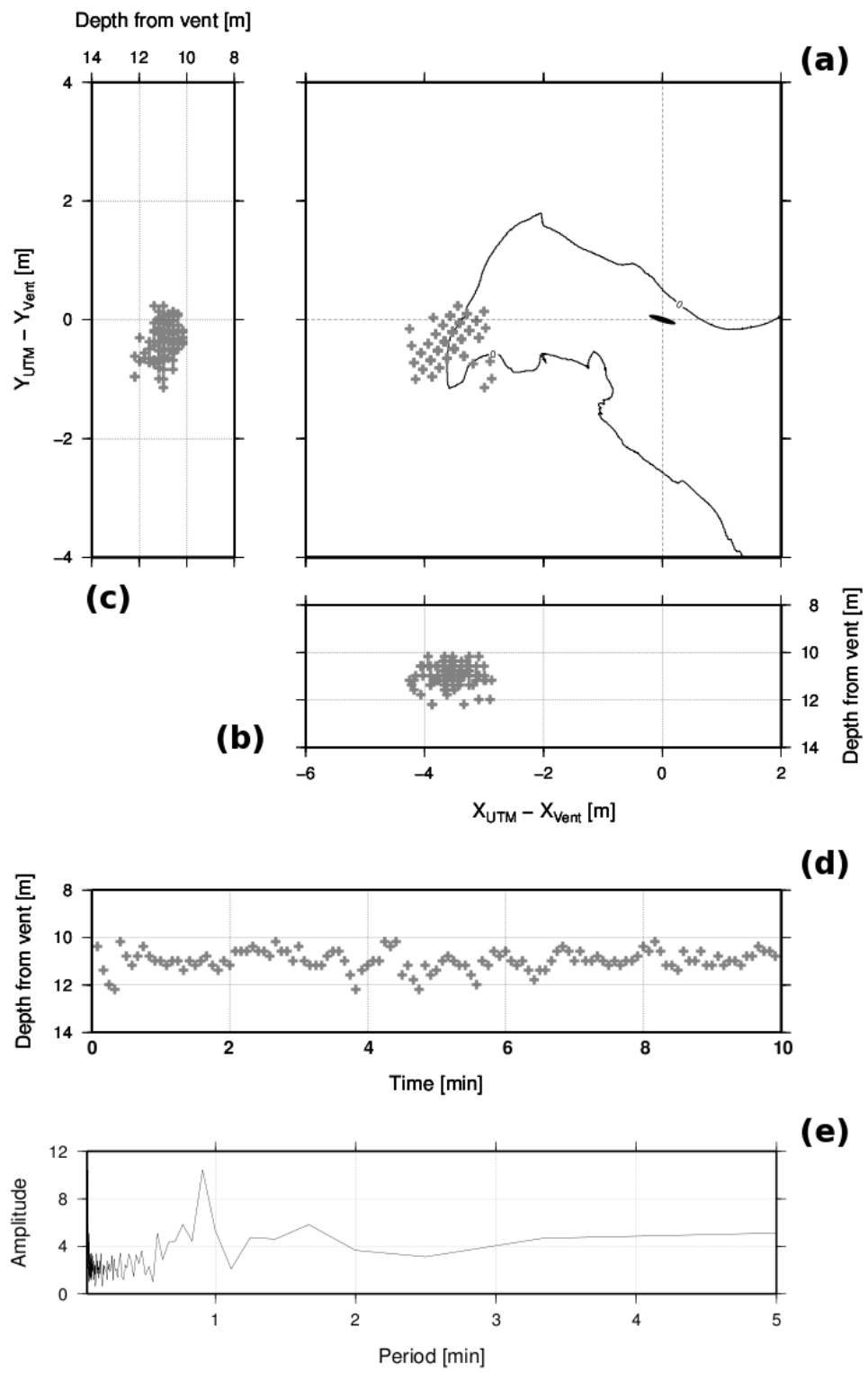


Figure 9